



Drying Dynamics of Solution-Processed Perovskite Thin-Film Photovoltaics: In Situ Characterization, Modeling, and Process Control


Simon Ternes,* Tobias Börnhorst, Jonas A. Schwenzer, Ihtez M. Hossain, Tobias Abzieher, Waldemar Mehlmann, Uli Lemmer, Philip Scharfer, Wilhelm Schabel, Bryce S. Richards, and Ulrich W. Paetzold*

A key challenge for the commercialization of perovskite photovoltaics is the transfer of high-quality spin coated perovskite thin-films toward applying industry-scale thin-film deposition techniques, such as slot-die coating, spray coating, screen printing, or inkjet printing. Due to the complexity of the formation of polycrystalline perovskite thin-films from the precursor solution, efficient strategies for process transfer require advancing the understanding of the involved dynamic processes. This work investigates the fundamental interrelation between the drying dynamics of the precursor solution thin-film and the quality of the blade coated polycrystalline perovskite thin-films. Precisely defined drying conditions are established using a temperature-stabilized drying channel purged with a laminar flow of dry air. The dedicated channel is equipped with laser reflectometry at multiple probing positions, allowing for in situ monitoring of the perovskite solution thin-film thickness during the drying process. Based on the drying dynamics as measured at varying drying parameters, namely at varying temperature and laminar air flow velocity, a quantitative model on the drying of perovskite thin-films is derived. This model enables process transfer to industry-scale deposition systems beyond brute force optimization. Via this approach, homogeneous and pinhole-free blade coated perovskite thin-films are fabricated, demonstrating high power conversion efficiencies of up to 19.5% (17.3% stabilized) in perovskite solar cells.

1. Introduction

In the last decade, hybrid metal-halide perovskites emerged as a new class of solution-processable semiconductors with excellent optoelectronic properties.^[1–3] While the initial advancement in this field was mostly driven by the material methylammonium lead iodide (MAPbI₃) perovskite, mixed-cation perovskites so-called double-, triple-, or quadruple-cation perovskites^[4–8] have come into focus in recent years. Devices based on mixed-cation perovskite thin-films demonstrate improved stability and higher power conversion efficiencies (PCE).^[4] Nevertheless, MAPbI₃ still remains the most studied reference material and is extensively characterized, both experimentally and theoretically. The material exhibits a broad optical absorption with a bandgap of ≈1.55 eV as well as long excited charge carrier life times and diffusion lengths due to its high defect tolerance.^[9–12] The discovery of the beneficial optoelectronic properties of hybrid perovskites has tremendous impact on a large range of optoelectronic technologies,^[13–17] among which perovskite thin-film photovoltaics (PV) are very prominent.^[3,18]

S. Ternes, I. M. Hossain, Prof. U. Lemmer, Prof. B. S. Richards, Dr. U. W. Paetzold
Institute of Microstructure Technology
Karlsruhe Institute of Technology
Hermann-von-Helmholtz-Platz 1, 76344 Eggenstein-Leopoldshafen, Germany
E-mail: simon.ternes@kit.edu; ulrich.paetzold@kit.edu

 The ORCID identification number(s) for the author(s) of this article can be found under <https://doi.org/10.1002/aenm.201901581>.

© 2019 The Authors. Published by WILEY-VCH Verlag GmbH & Co. KGaA, Weinheim. This is an open access article under the terms of the Creative Commons Attribution License, which permits use, distribution and reproduction in any medium, provided the original work is properly cited.

The copyright line for this article was changed on 6 September 2019 after original online publication.

DOI: 10.1002/aenm.201901581

S. Ternes, J. A. Schwenzer, I. M. Hossain, T. Abzieher, Prof. U. Lemmer, Prof. B. S. Richards, Dr. U. W. Paetzold
Light Technology Institute
Karlsruhe Institute of Technology
Engesserstr. 13, 76131 Karlsruhe, Germany

S. Ternes, T. Börnhorst, W. Mehlmann, Dr. P. Scharfer, Prof. W. Schabel
Institute of Thermal Process Engineering–Thin Film Technology (TFT)
Karlsruhe Institute of Technology
Kaiserstr. 12, 76131 Karlsruhe, Germany

Perovskite solar cells experienced an extraordinary increase in PCE from $\approx 3.8\%$ in 2009^[19] to over 24% in 2019.^[20] This increase was accompanied by an increased control of the morphology formation of the spin coated perovskite thin-films.^[21–23] However, the process transfer to large-scale coating techniques is complex and the PCEs of large-scale perovskite solar modules still lack behind.^[24,25] Clearly, there is a need for a better understanding of the perovskite thin-film formation process from the deposited precursor solution thin-film toward the final polycrystalline thin-film morphology that is incorporated into the devices. Common problems of perovskite thin-films fabricated by scalable solution-processed deposition techniques are a high roughness and high pinhole densities.^[26–32] The challenges with scalable deposition arise from thicker and less homogeneous solution films compared to spin coated solution films that are smoothened by sheer forces during the entire perovskite formation process prior to annealing.^[33] The resulting increased drying time and high solvent content in these films magnify the impact of drying related transport phenomena such as the coffee ring effect and Marangoni convection along with inhomogeneous crystal growth kinetics.^[34] However, rapid drying as induced by air quenching,^[30,35–41] high substrate temperatures,^[42–47] vacuum annealing,^[48–50] or anti-solvent quenching^[29,51] is reported to significantly improve the perovskite thin-film morphology. All rapid drying methods have in common that they induce a prompt crystallization in the thin-film by a fast change in environment parameters. However, to date, the fundamental understanding of the physical processes present during the drying of the solution film and the associated formation of perovskite thin-films is missing.

In first studies, the drying dynamics of perovskite solution thin-films have been investigated via different in situ measurement techniques such as photoluminescence,^[52,53] X-ray diffraction,^[38,41,46,54–59] spectral absorption,^[41,52] optical microscopy,^[38,41,46,60] chromatography,^[54] and interferometry.^[56] These studies mostly reach consensus on the discrimination of the following essential processing steps:

- I. Coating–deposition of a precursor solution thin-film;
- II. Drying–solvent transport out of the film;
- III. Nucleation–formation of crystalline colloids through supersaturation;
- IV. Crystal growth–growing of crystalline colloids and formation of crystalline grains.

The final perovskite thin-film morphology is affected by each of these processing steps, which implies that the resulting device performance requires a careful optimization and controlled manipulation of each processing step. One way to realize this is a brute force optimization of the parameter space each time a new coating technique is established in the field of perovskite PV. Alternative, more efficient routes for designing optimized deposition processes and tools would require a sophisticated model of the perovskite formation process. On the one hand, such a model must provide quantitative predictions of the required environmental parameters and, on the other hand, it must have general applicability beyond a single specific coating technique.

For obtaining a general understanding of the perovskite thin-film formation, environmental parameters, like the gas and

substrate temperature as well as the air circulation, need to be controlled precisely. While the substrate temperature is well-defined in most reported perovskite fabrication routines,^[31,32,42,61–63] so far, not many studies have been published on a simultaneous exact control of the gas temperature and the convective drying conditions. Therefore, the gaseous transport of solvent from the film surface can vary significantly depending on the geometry of the used surrounding air circulation system, such as glove boxes or fume hoods, which impact reproducibility and process transfer.^[35] In 2017, two groups examined the impact of a well-defined laminar air flow on drying solution films during the fabrication of perovskite PV. They presented first results on monitoring and modeling the drying process: Gao et al. demonstrated that the morphology of the perovskite thin-film can be optimized by adjusting the air flow velocity and temperature over the substrate.^[64] A comparable approach was proposed by Remeika et al. who reported on the optimization of spray-coated PbI_2 -films for the fabrication of perovskite solar cells in a channel with laminar air flow.^[65] Additionally, Remeika et al. monitored the PbI_2 -solution film thickness by laser reflectometry for validating their drying model. In order to advance these studies and develop an in-depth understanding, there is a need for a combined approach of both precise in situ measurements and quantitative modeling of the perovskite thin-film formation, ensuring an environment with exactly defined drying conditions.

In this work, we report on blade coated MAPbI_3 precursor films in a laminar flow channel monitored by laser reflectometry on multiple probing positions. With this approach, we acquire a general understanding of process transfer, ruling out the influence of undefined environmental parameters and different coating geometries. We develop a quantitative model that accurately describes the evolution of the solution thin-film thickness. This model enables predictions beyond the coating and drying setup used in our study as it applies to all drying geometries where the mass transfer coefficients are tabulated. We propose this methodology as a new standard in the field of perovskite PV in order to significantly reduce the necessary extent of experimental re-optimizations that would require intense personnel and financial efforts. Our goal is to pave the way toward efficient transfer strategies of perovskite fabrication routines from the lab-scale spin coating process to industrial-scale coating techniques.

2. Results and Discussion

2.1. Controlling and In Situ Monitoring of the Perovskite Precursor Drying Process

Herein, we introduce a combined method of process transfer: controlling the drying process of the precursor solution thin-film with precisely defined environmental parameters and, at the same time, monitoring of the drying dynamics during the process of perovskite formation. In order to realize this drying control and monitoring, a flow channel setup is used as designed by Schmidt-Hansberg et al.^[66–69] (see **Figure 1a**). The flow channel ensures well-defined drying conditions by a laminar air flow over the substrate and temperature stabilization of the air and the channel walls as well as the stage holding the

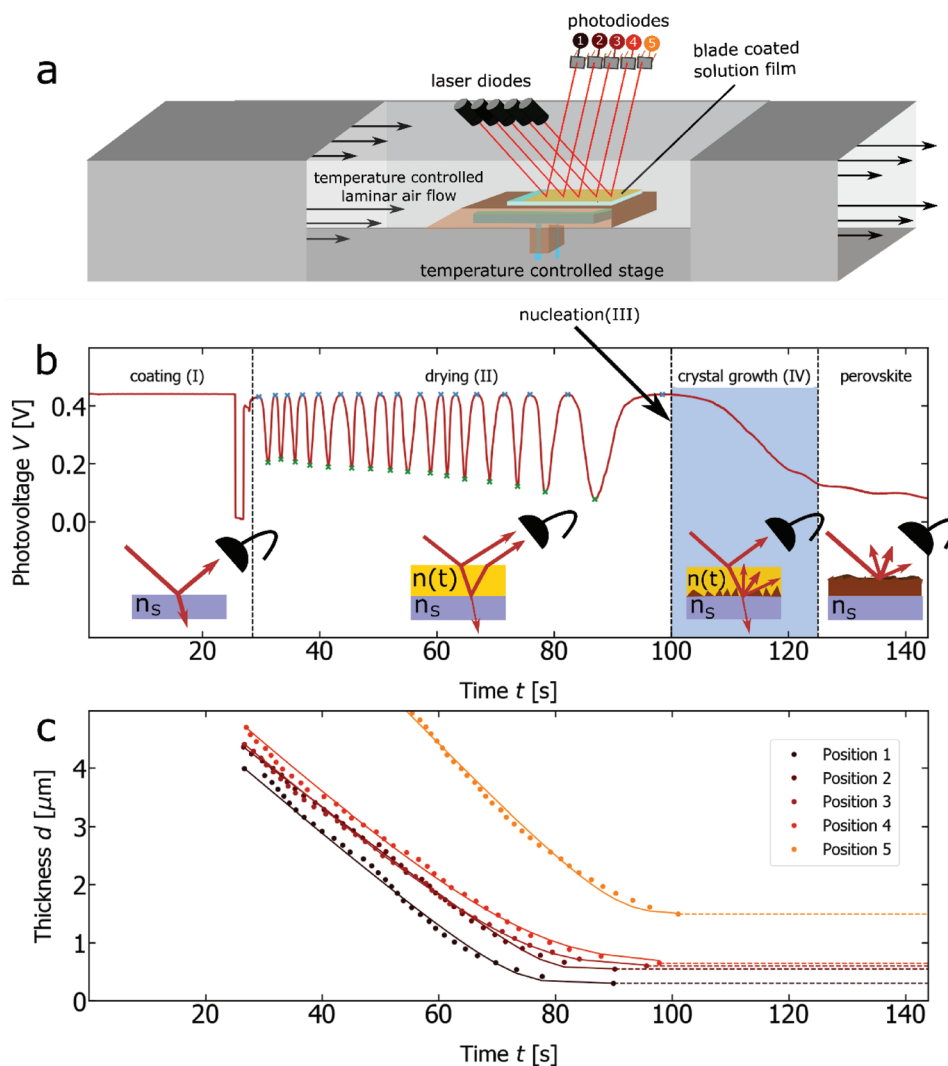


Figure 1. a) Schematic depiction of the flow channel setup (For photographs see Figures S1 and S2 in the Supporting Information). Five laser diodes probe the reflectivity of the deposited solution layer as it dries. b) Typical recorded photovoltage signal of the photodiode at position 3 during the drying of a perovskite solution layer. The different steps coating (I), drying (II), nucleation (III) and crystal growth (IV) of the deposition process can be identified from the signal shape. The blue shaded region is the timespan of crystal growth as investigated further in Figure S11 (Supporting Information). c) Thickness evolution as calculated from the signals of the five photodiodes as depicted in (a). The calculation is based on the temporal position of the extrema as obtained from the oscillating signal in (b). The differences in the height of the final film thickness and the initial solution thicknesses are attributed to coating inhomogeneities on the substrate edge. Position 5 furthermore exhibits different drying dynamics as compared to the four other positions because of irregular movements of the drying front (see Figures S6 and S7 in the Supporting Information). The solid lines are fits of the precursor drying model as introduced in Section 2.3.

substrate. Setting these precise constraints on the environment parameters is required for quantitative modeling of the particle transfer in the system, ruling out the impact of unknown convective or heat-transfer processes. In situ monitoring of the film drying is realized by five diode laser probes and five photodiodes, recording the respective reflected laser beam intensity over time. During the perovskite thin-film formation process, the photodiode signals follow a typical shape, as can be seen in Figure 1b. First, at the blade coating step (I), the blade is dragged over the substrate, interrupting the laser beam reflected on the substrate surface for a short time. Subsequent to the coating, the laser light impinges on the drying perovskite solution thin-film (II). The thickness-dependent

thin-film interference induces oscillations in the reflected laser light intensity as the thin-film shrinks upon the evaporation of solvent. After the drying, the light intensity impinging on the photodiode falls off until it reaches a base-level. This intensity drop is attributed to the continuously increasing nucleation of crystalline colloids in the supersaturated solution. When these colloids start growing, they scatter an increasing quantity of the light, further reducing the specularly reflected light intensity (III). Subsequently, these crystalline seeds grow until the base-level is reached (IV). The magnitude of the base-level is determined by the roughness of the perovskite surface reflecting the laser beam, since the transmitted laser beam is attenuated by the light absorption in the perovskite

thin film. We note that, following this crystal growth process, crystal recovery and (re)crystallization is driven further by an additional annealing step influencing the internal crystalline structure of the perovskite film ($T = 115\text{ }^{\circ}\text{C}$). These internal structural changes cannot be resolved by reflectometry, since the film is no longer transparent.

Each respective maximum and minimum—the extremum occurring in the reflectivity of the drying thin-film—can be assigned an integer, m , which defines its “order of interference.” If the interference order is known for a particular extremum, m_{ref} , the orders of all other extrema are pinned because m simply increments by 1 from one extremum to the next. Herein, we measure the film thickness of the dried perovskite thin-film, d_{dry} , by profilometry in order to approximate a reference extremum order m_{ref} as assigned to the last maximum in the photovoltage signal. At every respective extremum position in time, t_m , the absolute values of the thickness, $d_m(t_m)$, is accordingly calculated in terms of the corresponding interference order, m . The detailed calculation is provided in the Supporting Information. This reflectometry method is well-established in the field of organic thin-film processing^[66,68,70–73] and can be applied in an arbitrary industrial-scale dryer with a working distance greater than about 1 cm^2 . In this work, we demonstrate the applicability of this method for the drying of the perovskite solution film (II) just before the nucleation (III). Typical resulting drying curves for each probing position are depicted in Figure 1c.

It should be noted that the positions 1–5 are oriented along the air flow direction. As a consequence, the solvent content in the air flow increases, the concentration boundary layer thickness, ΔS_{bnd} , increases and the drying rate decreases from position 1 to position 5. Additionally, the drying rate is influenced by inhomogeneities in the initially deposited thickness of the solution film and nonuniform movement of the drying front (see Figures S6 and S7, Supporting Information). Position 5 is located at the end of the substrate where these irregularities considerably impact the drying rate.

2.2. Discriminating Different Stages of the Perovskite Precursor Drying

When analyzing the thickness evolution recorded by laser reflectometry as explained above, we first focus on discriminating the fundamental drying dynamics in different stages of the perovskite precursor drying (Figure 2). For this purpose, the thickness evolution of two different *N,N*-dimethylformamide (DMF)-based MAPbI_3 perovskite precursors are compared to the drying of a pure DMF-film, ensuring equal drying and coating parameters. The first precursor is the classical equimolar PbI_2 :MAI precursor. The second precursor is based on an optimized recipe as developed by Qiu et al.^[74] It contains two different lead sources, lead(II) acetate trihydrate, $\text{Pb}(\text{CH}_3\text{COO})_2 \cdot 3\text{H}_2\text{O}$ (abbreviated as PbAc_2), and lead(II) chloride (PbCl_2), mixed in the ratio 4:1, while the ratio of Pb to MAI is fixed at 1:3.

In a first drying stage (A), the molar fraction of DMF molecules with respect to the sum of DMF molecules and perovskite unit cells, \tilde{x}_i , in the film is very close to one, such

that the drying dynamics of the two precursor solution films are equivalent to those of a pure DMF solvent film. In a second drying stage (B), \tilde{x}_i falls off so far that the evaporation in the precursor films is exponentially slowed down as compared to the pure DMF-film. This deceleration of the precursor drying was previously reported by Munir et al.,^[56] who performed in situ white light interferometry on spin coated precursor films. Notably, since we measure on nonspinning substrates, we are able to rule out the possibility that the slowing-down is (partially) caused by viscosity changes upon drying. According to Munir et al., the reason for the deceleration are solvent–solute interactions.^[56] However, in the model presented here, we describe the deceleration of the drying speed before the nucleation solely by a decrease in \tilde{x}_i . Thereby, we impose the simplest possible assumptions: First, we suppose that there is approximately an ideal solvent–solute mixture in the film, where \tilde{x}_i is constant in the vertical direction of the film. Second, we assume that there is no solute–solvent interaction at all times. Third, we assume that the air flow does not push the liquid film over the substrate, which is justified by a measurement of the final perovskite thicknesses along the air flow direction for different air speeds (Figure S19, Supporting Information). For the subsequent modeling, we make use of fundamental relations from the field of chemical process engineering, as already introduced by Schmidt-Hansberg et al. to the community of organic PV.^[66–69]

2.3. Modeling of the Perovskite Precursor Thin-Film Drying

The development of a quantitative model of the perovskite thin-film drying is essential for the understanding of thin-film processing in large-scale coating techniques. Once a model prediction can be expressed in terms of general quantities, which are tabulated in standard literature on drying machines,^[75] it is possible to determine suitable processing windows for arbitrary coating and drying machines. A similar approach has been successfully demonstrated for organic PV by Schmidt-Hansberg et al.^[69] The first step of modeling is a detailed analysis of the fundamental drying kinetics in the precursor solution thin-film. First of all, we note that in both drying stages A and B, there is no significant difference between the classical equimolar precursor recipe and the optimized lead chloride/lead acetate precursor by Qiu et al.^[74] (Figure 2), since the relative difference is below the accuracy of the reflectometry technique. This indicates that the evaporation of volatile byproducts such as MACl_2 does not significantly contribute to the observed drying dynamics as to the accuracy of the used reflectometry technique. As a consequence, we focus on the evaporation of DMF as main volatile component.

The transfer of gaseous DMF into the bulk drying gas can be described by Fick’s first law of diffusion—the general setting of a gaseous component i diffusing with the diffusivity δ_{ij} into the carrier gas j . Thereby, the molar fraction of i in the gas just above the surface of the film, $\tilde{y}_{i,\text{ph}}$, falls off to the molar fraction of i in the fresh drying gas $\tilde{y}_{i,\infty}$ within the concentration boundary layer thickness, ΔS_{bnd} (see schematic in Figure 2). Fick’s first law of diffusion then takes the form

$$j_{ij} = -\delta_{ij} \cdot \tilde{\rho}_{i,g} \cdot \frac{(\tilde{y}_{i,\text{ph}} - \tilde{y}_{i,\infty})}{\Delta S_{\text{bnd}}} \equiv -\beta_{ij} \cdot \tilde{\rho}_{i,g} \cdot (\tilde{y}_{i,\text{ph}} - \tilde{y}_{i,\infty}) \quad (1)$$

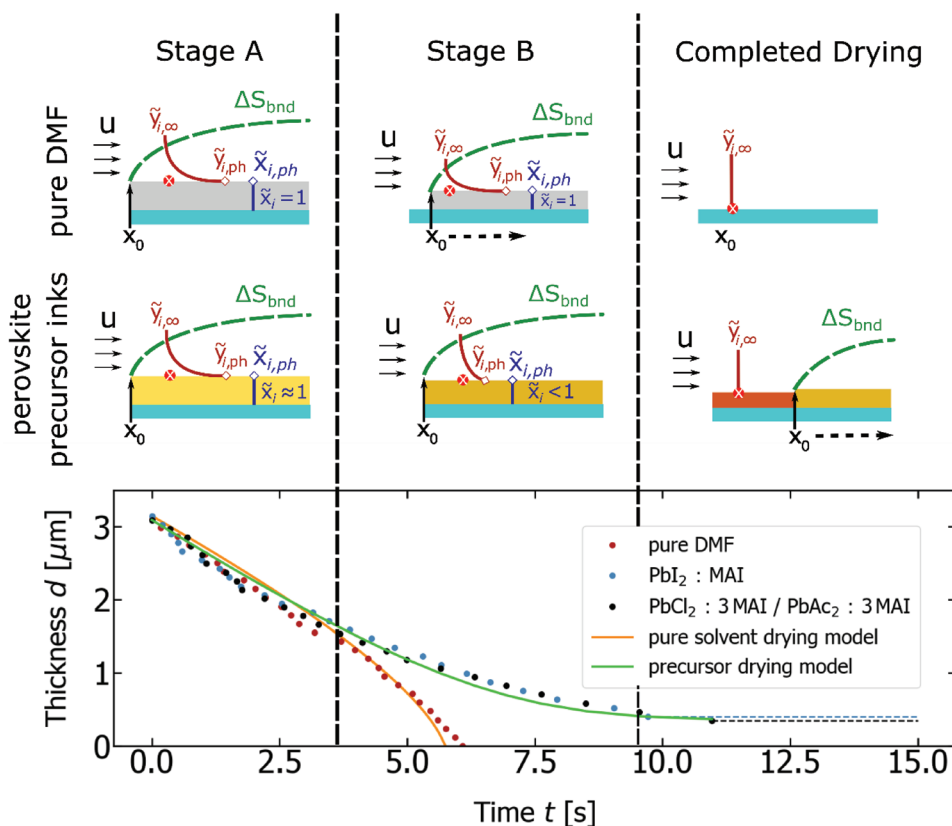


Figure 2. A typical thickness evolution upon drying of the thin-film as measured at 45 °C, with an air flow velocity of 0.2 m s⁻¹, a coating velocity of 8.3 mm s⁻¹ and a blade gap of 100 μm. Solution film of pure DMF (red), a precursor with PbI₂ and MAI in equimolar ratio (blue) and the mixed precursor of PbCl₂: 3MAI and Pb(CH₃COO)₂: 3MAI in the molar ratio of 1:4 (black). The drying of the pure DMF-film is accurately described by a linear drying model with a moving drying front (orange line) as described by Schmidt Hansberg et al.^[68] In the initial drying stage A, the perovskite precursor drying asymptotically aligns with the drying curve of the pure DMF film. In the late drying stage B, the drying dynamics in the perovskite precursors however exhibit an exponential deceleration, deviating from the drying curve of the DMF-film. The molar fraction of gaseous solvent over the film, $\tilde{y}_{i,ph}$ in stage B is lower as compared to the pure DMF-film, which is caused by a decrease of the molar fraction of liquid DMF molecules in the film, \tilde{x}_i . The precursor drying model accounts for this decrease as introduced in Section 2.3. (green line). The dashed green line in the pictograms shows the concentration boundary layer thickness ΔS_{bnd} defining the distance from the film surface at which the concentration of solvent in the bulk gas $\tilde{y}_{i,\infty}$ is reached.

where j_{ij} is the molar solvent flux of i from the film surface into the carrier gas, $\tilde{\rho}_{i,g}$ is the molar density of gaseous solvent, and the mass transfer coefficient is defined as $\beta_{ij} = \delta_{ij} / \Delta S_{bnd}$. As shown by Schmidt-Hansberg et al., β_{ij} can be parameterized with Sherwood correlations by the distance from the substrate edge, x , the distance from the drying front, x_0 , the Schmidt number, Sc , and the local Reynolds number, Re_x (for details see the Supporting Information).^[68] Furthermore, since the gas transport dynamics are comparatively slow compared to the dynamics of molecular evaporation out of the film surface, we can assume a thermodynamic equilibrium of the liquid–gas phase transition at the film surface at all times. This assumption is a common standard in drying engineering,^[76] which allows for expressing $\tilde{y}_{i,ph}$ by the molar ratio of i in the liquid solution on the film surface, $\tilde{x}_{i,ph}$, using Raoult's law as

$$\tilde{y}_{i,ph} = \gamma_i \cdot \frac{p_i^*}{p} \cdot \tilde{x}_{i,ph} \quad (2)$$

where γ_i is the activity coefficient, p_i^* is the vapor pressure of the pure solvent, and p is the pressure of the gas phase in the drying channel. According to the ideal gas law, we have $p = \tilde{\rho}_{i,g} RT$. As

mentioned in the last section, we choose the simplest possible assumption of an ideal solution with no solute–solvent interaction with $\gamma_i = 1$ and simplify further by assuming no concentration gradient in vertical direction, which will be justified in the following section by an assessment of the model fitting. Consequently, $\tilde{x}_{i,ph} = \tilde{x}_i = n_{i,l} / (n_{i,l} + n_{pvk})$ holds true in the film at all times, with the number of moles of solvent molecules per unit volume, $n_{i,l}$, and the number of moles of perovskite unit cells in the solution per unit volume, n_{pvk} . With the relations $j_{ij} = \tilde{\rho}_{i,l} \cdot dd/dt$ as well as $n_{i,l} = \tilde{\rho}_{i,l} \cdot (d - d_{dry})/d$ and $n_{pvk} = \tilde{\rho}_{pvk} \cdot d_{dry}/d$, we can express Equation (1) in terms of the time dependent film thickness, $d(t)$, for an unloaded drying gas ($\tilde{y}_{i,\infty} = 0$) as

$$\frac{dd}{dt} = -\beta_{ij} \cdot \frac{p_i^*}{\tilde{\rho}_{i,l} RT} \cdot \left(1 + \frac{d_{dry}}{d(t) - d_{dry}} \cdot \frac{\tilde{\rho}_{pvk}}{\tilde{\rho}_{i,l}} \right)^{-1} \equiv \frac{-r_i}{1 + d_s / (d(t) - d_{dry})} \quad (3)$$

where d_{dry} is the thickness of the dry perovskite film, $\tilde{\rho}_{i,l}$ is the molar density of the liquid component i in the film, and $\tilde{\rho}_{pvk}$ is the molar density of the perovskite material in the film. For the sake of shortening the notation of the modeling equations, we define $r_i = \beta_{ij} \cdot p_i^* / \tilde{\rho}_{i,l} RT$ as the drying rate of the pure component

i. Furthermore, we set $d_s = d_{\text{dry}} \tilde{\rho}_{\text{pvk}} / \tilde{\rho}_{i,1}$ as the dry film thickness stretched by the molar densities. Solving Equation (3) for $d(t)$ results in a simple analytic expression for the thickness evolution during the drying process

$$d(t) = d_{\text{dry}} + d_s \cdot W\left(\exp\left[-\frac{r_i}{d_s}t + C\right]\right) \quad (4)$$

where W is the Lambert W -function satisfying $z = W(z e^z)$ for all (complex) numbers, z . This model exhibits a correct asymptotic behavior. For $x \gg 1$, we have $W(x) \equiv \ln x$ and thus $d(t) \equiv d_{\text{dry}} - r_i t + d_s C$ for $t \rightarrow -\infty$, which is an accurate description of the drying stage A with a de facto constant drying rate in the region where the molar fraction of DMF molecules in the film, \tilde{x}_i , is close to 1. In the case $x \ll 1$ we find however $W(x) \equiv x$ and thus

$$d(t) \equiv d_{\text{dry}} + d_s \cdot \exp\left[-\frac{r_i}{d_s}t + C\right].$$

This exponential decay describes accurately the deceleration of the drying speed in drying stage B as caused by the reduction of \tilde{x}_i at the film surface. Hence, the model correctly describes the physical process dynamics of drying as measured by the reflectometry on the drying process in the perovskite solution thin-film (Figures 1c and 2). The parameter d_{dry} accounts for the final thickness at the investigated position. In case of an inhomogeneous film, it varies for each probing position (Figure 1c).

2.4. Assessment of the Prediction Power of the Derived Drying Model

The validity of the above derived model can be assessed by testing its predictive power for reproducing drying curves of various environmental parameter sets. For the assessment, an extensive parameter study is conducted, varying the temperatures from 25 to 85 °C in steps of 10 °C and the air flow velocity in logarithmic steps as 0.02, 0.2, and 2 m s⁻¹. This parameter range is chosen such that the drying dynamics take at least 5 s of time, which is required for analyses of the drying dynamics before the onset of the nucleation process. The maximum air speed of 2 m s⁻¹ originates from the boundary condition that we work with temperature stabilized dry air. For each parameter combination, the drying curves of the five positions are recorded. Subsequently, the initial five sample points of each respective drying curve are fitted with a simple linear regression method to extract the drying rate mean $\Delta d/\Delta t$ in the drying stage A of de facto linear drying (see Figure 3). The resulting values are in good agreement with the theoretical prediction for a pure DMF system, r_d , obtained from the Sherwood-correlations. The slopes in drying stage B decrease exponentially such that the trends are retained in a fit of the last three sample points (see Figure S8 in the Supporting Information). Consequently, we can adjust the average drying rate in the drying stage B by the air flow, suggesting that there is no significant mass transport limitation by DMF solvent diffusion from the inside of the film to the film surface (as to the accuracy of the reflectometry technique used herein). This experimental finding justifies the assumption that the solvent-solute mixture in the film is close to ideal at all times, i.e., there is approximately no concentration gradient of DMF along the vertical axis within the film.

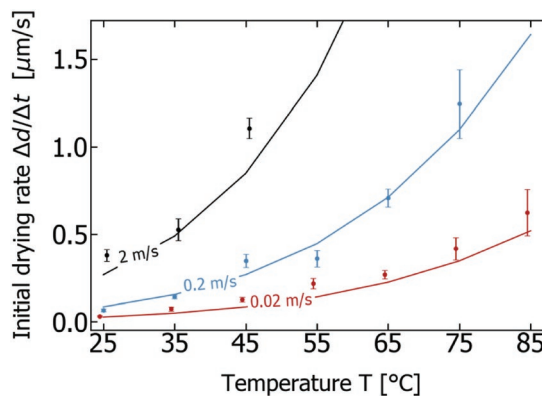


Figure 3. Mean and standard error of the measured drying rates in the first five sample points of drying stage A as compared to the predicted drying rate in drying stage A from the Sherwood correlations, r_i (solid lines). Because of the irregular lateral movement of the drying front (see Figures S6 and S7 in the Supporting Information), an average of the characteristic lengths $x_0 = 10$ cm and $x_0 = 20$ cm is assumed.

Pursuing further the analysis, the precursor drying model (introduced in Section 2.3) is fitted to the drying curves for each parameter set. Thereby, the constant C is fixed such that $d(0)$ equals the intercept of the linear regression, i.e., the initial thickness of the solution film, while d_s is left as a free fitting constant. From these results we can extract $d_s/d_{\text{dry}} = 0.47 \pm 0.07$ for the dataset excluding the 0.02 m s⁻¹ series (see Figure S9 in the Supporting Information). From literature, we find $\tilde{\rho}_{i,1} = 1.3 \times 10^{-2}$ mol mL⁻¹ for DMF and with the perovskite lattice constant at 300 K of $a = 6.3$ Å as measured by Whitfield et al.,^[77] we can calculate $\tilde{\rho}_{\text{pvk}} = 6.6 \times 10^{-3}$ mol mL⁻¹. Hence, the value d_s/d_{dry} as obtained from the fitting is in agreement with the theoretical prediction $\tilde{\rho}_{\text{pvk}}/\tilde{\rho}_{i,1} = 0.51$. The accuracy-of-fit parameters can be found in the Supporting Information (see Figure S10 in the Supporting Information). This convergence of the free fitting parameter, d_s , with certified, fundamental material properties as reported in literature demonstrates the applicability of the methodology presented herein with an outstanding persuasive power. This quantitative confirmation of our predictive model uniquely expands the available knowledge of the perovskite thin-film formation process beyond pure empirical observations and qualitative process description.

2.5. Morphology Control Enables High Devices Performances

For relating the predictions of our quantitative model of the precursor drying with relevant properties of the resulting perovskite thin-films, we characterize the perovskite morphology and device performances for each tested parameter set. We find that the layer morphology and the solar cell PCE strongly depend on the applied control parameters, the air flows and temperatures (see Figures 4 and 5, additional details in Figures S12–S18, Supporting Information). By selecting accurate drying conditions, the PCE of the blade coated devices as measured by backward J - V -scans is improved from around 10% up to 19.5% (Figure 4), which results in a champion stabilized PCE of 17.3% (Figure 7). This increase in PCE clearly demonstrates the significance of exact drying control. If the air velocity is too

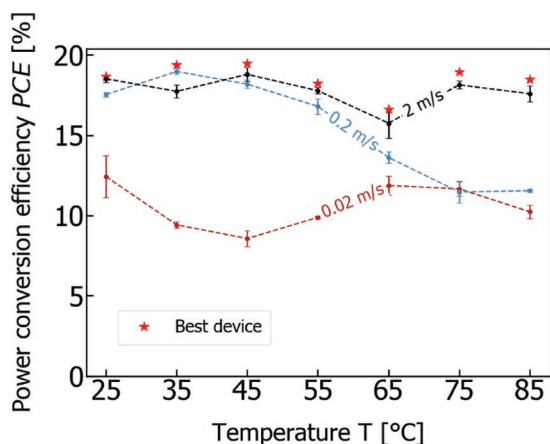


Figure 4. Mean and standard error of the PCEs from backward J - V -measurements (0.6 V s^{-1}) of the blade coated perovskite solar cells at the different processing parameters. The red stars designate the best device of all velocities at the respective temperature. The corresponding values of J_{SC} , V_{OC} , fill factors, and backward PCE are found in Figures S12–S15 (Supporting Information). The stabilized PCE are significantly lower (Figure 8). In this figure, the data of four repeated experiments is plotted.

low ($\approx 0.02 \text{ m s}^{-1}$) the thin-films exhibit pinholes and a high roughness for all tested temperatures being detrimental for the PCEs of the devices (Figures 4 and 5). For high air velocities ($\approx 2 \text{ m s}^{-1}$), the films are however nearly pinhole-free with a root mean square (RMS) roughness of about 30 nm for all investigated temperatures (Figure 5 and Figure S18, Supporting Information). In the intermediate case ($\approx 0.2 \text{ m s}^{-1}$), pinhole free films are obtained at temperatures up to 55 °C, while the pinhole density and the roughness heavily increase at higher temperatures starting from 65 °C (Figure 5 and Figure S18, Supporting Information). The increase in the pinhole density is directly correlated with a PCE drop (see Figures 4 and 5) that is attributed to a reduction in the fill factor mainly caused by shunt resistance (see Figure S14 in the Supporting Information). However, the fill factor saturates at around 60%, due to the robustness of layer sequence ETL/perovskite/Spiro-OMeTAD toward pinhole densities around 1% in the perovskite thin-film.^[74] We note that the grain sizes do not exhibit a significant trend in our study, most probably due to irregularities of the deposited solution layer (coated wet layer thickness, concentration, stoichiometric error) or the homogeneity of air flow (varying local air flow velocities). However, we find no correlation between the device efficiencies and the measured grain sizes (see Figure 4 and Figure S17, Supporting Information).

Interestingly, our study not only demonstrates the beneficial impact of gas quenching for process upscaling, but also implies that high drying rates do not necessarily yield favorable perovskite thin-film morphologies. For example, the drying rate at the air flow velocity of 0.02 m s^{-1} and the temperature of 85 °C is higher than the drying rate at 2 m s^{-1} and 25 °C, but the PCEs obtained by the first parameter set are much lower than those obtained by the second (see Figures 3 and 4). This fact indicates that there is a difference in controlling the drying rate by temperature on the one hand and air velocity on the other hand. While the air velocity mainly influences the speed of solvent removal from the film, i.e., the drying process (II),

the temperature influences the drying (II), the nucleation (III) and the crystal-growth (IV) processes because the diffusivity of ions in solution depends on the temperature.^[78] An empirical evidence for these relations is the fact that the timespan of the crystal growth (blue shaded in Figure 1) depends mainly on the applied temperature (see Figure S11 in the Supporting Information), while the drying rate depends both on the temperature as well as the air flow velocity (Figure 3). The higher the temperature, the more the crystal growth of nucleated seeds is fostered such that they finally grow to large isolated crystallites, leaving areas with almost vanishing thickness in between (see Figure 5 and Figures S16 and S17, Supporting Information). For obtaining a homogeneous, pinhole-free perovskite thin-film morphology, the solvent removal as controlled by the convective air flow must be fast, driving the system quickly above supersaturation and, thus, inducing a high nucleation rate before the isolated crystallites have enough time to form. Consequently, pinhole free films can either be obtained by lowering the temperature to suppress the crystal growth dynamics by “freezing” (see 0.2 m s^{-1} series) or by choosing sufficient air velocity to induce rapid supersaturation at a particular temperature (see 2 m s^{-1} series). This qualitative, empirical finding is in good agreement with other studies on perovskite thin-film fabrication.^[36,38,41,46,56] However, as to our knowledge, we report on a quantitative drying model along with favorable processing parameters for the first time in the field of perovskite PV. In order to generalize the processing window as given here in terms of the air flow velocity, one needs to consider the corresponding mass transfer coefficients, β_{ij} , as given by the Sherwood-Correlations (see Equation S2 in the Supporting Information). We obtain for the air velocities of 0.02, 0.2, and 2.0 m s^{-1} , the respective mean mass transfer coefficients $(8.7 \pm 2.5) \cdot 10^{-3} \text{ m s}^{-1}$, $(2.8 \pm 0.8) \times 10^{-2} \text{ m s}^{-1}$ and $(8.7 \pm 2.5) \times 10^{-2} \text{ m s}^{-1}$, which can be used to design arbitrary industrial-scale dryers (see Figures S4 and S5 in the Supporting Information).

2.6. Process Transfer from Blade Coating to Spin Coating

The performance of the solar cells fabricated by gas-assisted blade coating can be assessed in reference to equivalent solar cells with same stack, incorporating a spin coated (instead of a blade coated) perovskite absorber layer from the same precursor. The functional layers of the spin coated and blade coated devices were fabricated according to the same optimized spin coating recipes in order to ensure comparability on the device level between the two perovskite deposition methods. The J - V -scans and constant voltage power output of the champion devices for each coating technique are comparable, indicating optimal process transfer from spin coating to blade coating (see Figures 6 and 7 and Table 1). The statistical distribution of the PCEs is also similar, having comparable mean values and standard deviations (see Figure 8). Furthermore, we find that the J - V curves exhibit a high hysteresis for both techniques, indicating that the hysteresis is most likely not related to morphology but arises from bulk or interface properties of the MAPbI_3 as processed from solution. The stabilized PCEs of the blade coated devices

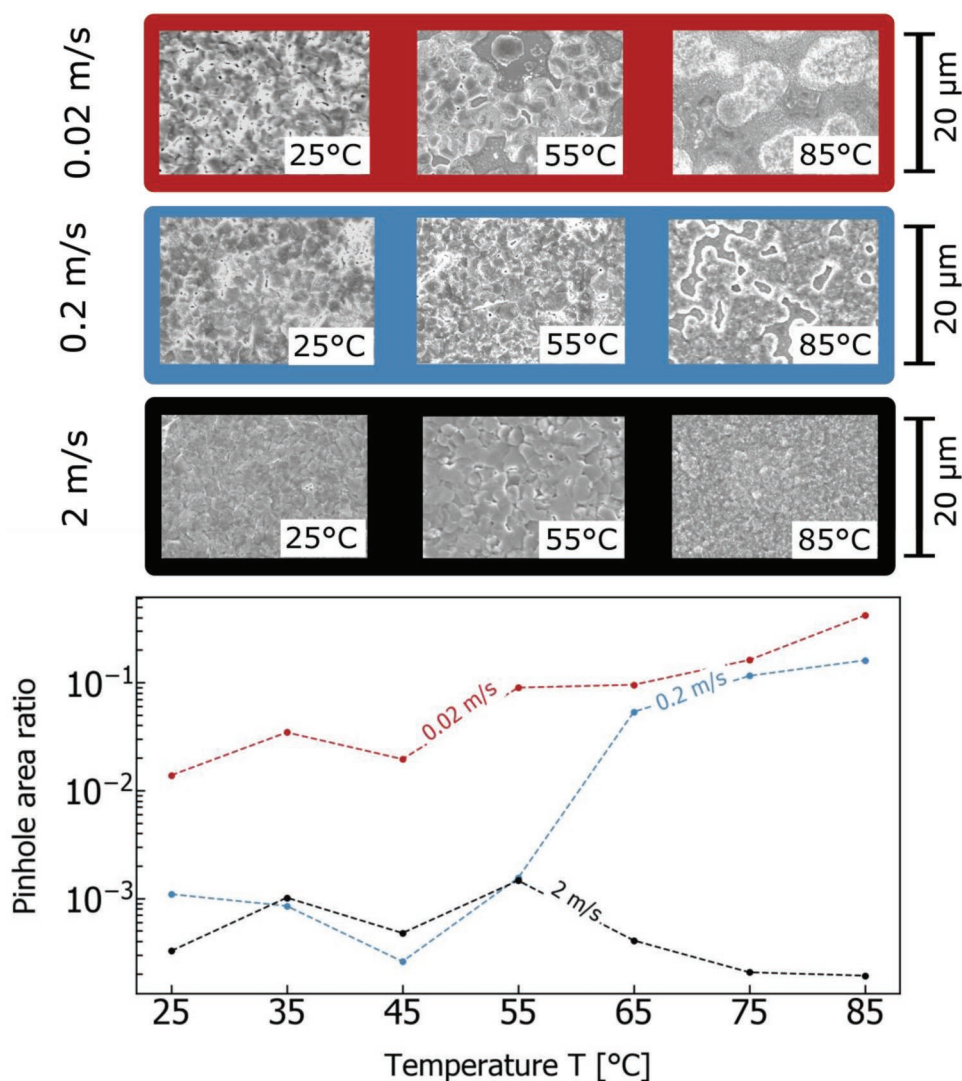


Figure 5. Ratio of the examined pinhole area with respect to the area covered with the perovskite thin-film. The pictures series depict typical SEM images at the covered temperature ranges. The exact and full morphology series is shown in Figures S16 and S17 (Supporting Information). The roughness as extracted from AFM correlates with the pinhole area ratio (see Figure S18 in the Supporting Information).

exhibit average and peak values of 15.5% and 17.3% respectively, which is on the state-of-the-art level for pure MAPbI₃ devices as reported by other groups with similar device fabrication methods.^[36,40,42,47,51,62] The stabilized PCE is a more reliable quantity than the PCEs as measured from *J*-*V*-curves, since it comes closer to the field operation of solar modules and eliminates the influence of short-time (<5 s) hysteresis phenomena.^[25]

3. Conclusion

In this work, we investigate systematically the drying of perovskite thin-films processed from solution under well defined drying conditions. With the blade coated perovskite layers dried in the temperature-stabilized flow channel, we are able to fabricate MAPbI₃ solar cells in a wide processing window (25–85 °C at 2.0 m s⁻¹) with a stabilized mean PCE of 15.5%

and a mean PCE of 17.0% in the backward current density–voltage (*J*-*V*) scan, reaching a champion stabilized PCE of 17.3% (19.5% in the backward *J*-*V* scan). Compared to entirely spin coated equivalent devices, these PCEs do not significantly deviate, which implies an optimal process transfer from spin coating to blade coating. In summary, we report that with exact control and monitoring of the drying step in the perovskite thin-film formation, the challenges of process transfer can be successfully met. We demonstrate furthermore that quantitative modeling of the drying process enables the prediction of the polycrystalline thin-film morphology. Since we provide precise calculations of the mass transfer coefficients, β_{ij} , the coating windows demonstrated herein can be easily translated into parameters of large-scale drying machines, using the model presented. The only premise is applying a different correlation for the calculation of β_{ij} , which are well-known within the field of process engineering.^[75,76] Furthermore, the simple, but powerful in situ reflectometry can be performed in any

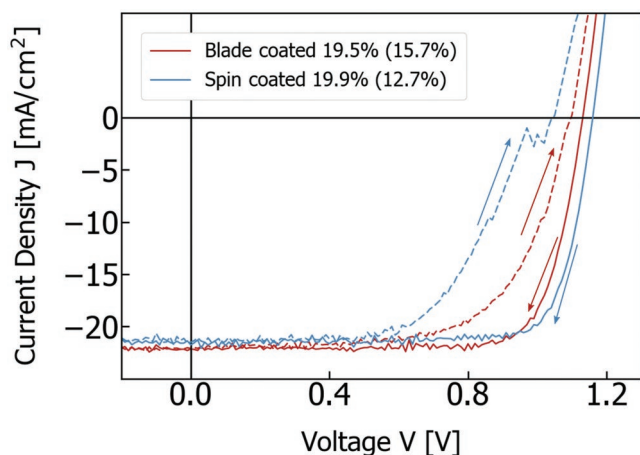


Figure 6. Comparison of the J - V -scans (0.6 V s^{-1}) of the two champion devices with spin and blade coated active layers. While the fill factors of the two J - V -curves are identical, the blade-coated sample has a slightly lower V_{OC} and a slightly higher J_{SC} . The exact values of the characteristic properties are listed in Table 1.

industrial scale dryer with a working distance over about 1 cm^2 . We propose that the methods described herein should become a standard for predicting the perovskite thin-film morphology in large-scale deposition systems.

4. Experimental Methods

Flow Channel Operation: The flow channel was operated in a fume hood and flushed with dry air from a 10 bar line. The air velocity was stabilized at 0.02 and 0.2 m s^{-1} using a mass flow controller (mks, PR4000B in combination with a 200slm 1579A00112 module) and a hot-wire anemometer (TSI Instruments Ltd., Airflow TA430-A) to measure the current air flow. For the 2 m s^{-1} measurements, the flow channel was directly connected to the 10 bar gas supply because the mass flow controller's maximum flow rate was too low. The air flows through the pipe of a thermostat (Lauda, RC20 CS) before it enters the 50 cm long channel, where the air stream is widened by a diffusor. The walls of the channel are temperature stabilized using an electrical temperature controller. The thermostat pumps the temperature stabilized water through the wing-shaped substrate stage such that the air and the table always have the same temperature.

Reflectometry Measurements: Just before the coating process, the data acquisition of the photodiode signals was started using a National Instruments acquisition board (USB-6259 BNC). The sampling rate was $100 \text{ points s}^{-1}$ per photodiode. The data acquisition was completed when all photodiode signals reached the base level after the last reflection (there is often a slight remaining drift) and the perovskite film turned brown. The substrates were then transferred to the annealing process (see next section). The laser probe diodes with a wavelength of 650 nm were supplied by a potentiometer to choose their power at maximum reflection (empty substrate) just below the saturation voltage

Table 1. Electrical characteristics of champion devices.

Dep. Method	PCE [%] (backw.)	PCE [%] (forw.)	PCE [%] (stab.) ^{a)}	J_{sc} [mA cm ⁻²]	V_{oc} [V] (backw.)	Fill Factor [%] (backw.)	V_{oc} [V] (forw.)	Fill Factor [%] (forw.)
Spin coated	19.9	12.7	17.5	21.6	1.16	78.8	1.05	56.7
Blade coated	19.5	15.7	17.3	22.1	1.13	77.8	1.10	64.8

^{a)}averaged over 250 s.

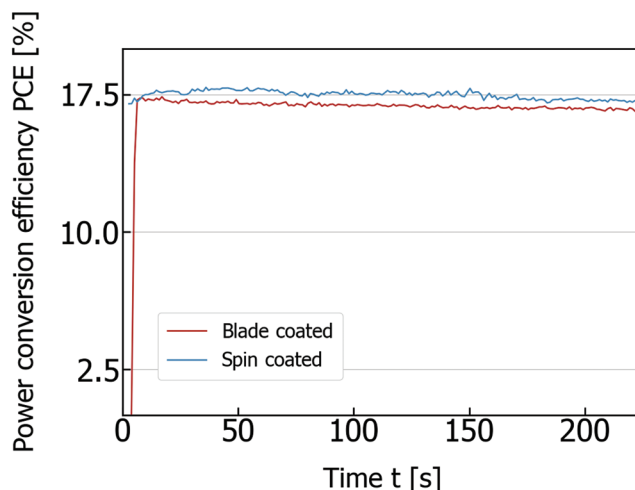


Figure 7. Comparison of the constant voltage power output of the two champion devices with spin and blade coated active layers. Both devices show a slight decrease in the measured PCE. The stabilized PCE values are comparable.

of the photodiodes. These probes were mounted on the removable cover around the substrate stage such that they impinge at the angle of 26° as measured with respect to the substrate normal. For high quality reflective measurements 4 in. silicon wafers were spin coated with tin oxide (SnO_2) nanoparticles and then cut into $6 \times 3 \text{ cm}^2$ substrates. While silicon had an optimal absorption/reflection-ratio to be used in the reflectometry measurements, the reflection on the indium tin oxide coated glass substrates as used for solar cell fabrication (see next section) was not high enough to obtain a sufficient signal to noise ratio.

Fabrication and Characterization of Perovskite Solar Cells: The fabricated solar cells had the planar architecture indium tin oxide (ITO)/ SnO_2 -nanoparticles/MAPbI₃/Spiro-MeOTAD/Au. Pre-patterned $64 \text{ mm} \times 64 \text{ mm}$ ITO substrates (Luminescence Technology, sheet resistance $15 \Omega \text{ sq}^{-1}$) were pre-cut in a 4×4 matrix on the glass-side. Then, the substrates were cleaned 10 min in an ultrasonic bath with acetone and isopropanol respectively and etched under an O_2 -plasma at 100 W for 3 min. Subsequently, SnO_2 nanoparticles colloidal dispersion (Alfa Aesar, 15%) was diluted to a concentration of 2%. The SnO_2 nanoparticle electron transport layer (ETL) was spin coated on the $64 \text{ mm} \times 64 \text{ mm}$ substrate at 4000 rpm for 30 s with the initial volume of $400 \mu\text{L}$ per substrate and annealed at $250 \text{ }^\circ\text{C}$ for 60 min. As a next step, each respective substrate was broken into two $32 \text{ mm} \times 64 \text{ mm}$ substrates. To improve the wettability, these substrates were again treated with O_2 plasma at low power of 30 W for 1 min.

To initiate the coating procedure, the cover of the substrate stage was removed from the channel and the blade (Zehntner, ZUA 2000 Universal Applicator) was placed for several minutes in the channel to heat it to the surrounding temperature. The blade was attached to a stepper motor with a wire, while the surface-activated substrate was placed on the stage in front of the blade. After dripping $15 \mu\text{L}$ of solution (PbCl_2 : 3MAI was added to PbAc_2 :3MAI solution (DMF) such that PbCl_2 : $\text{PbAc}_2 = 1:4$ and the lead concentration was $0.75 \text{ mol Pb mL}^{-1}$ DMF;

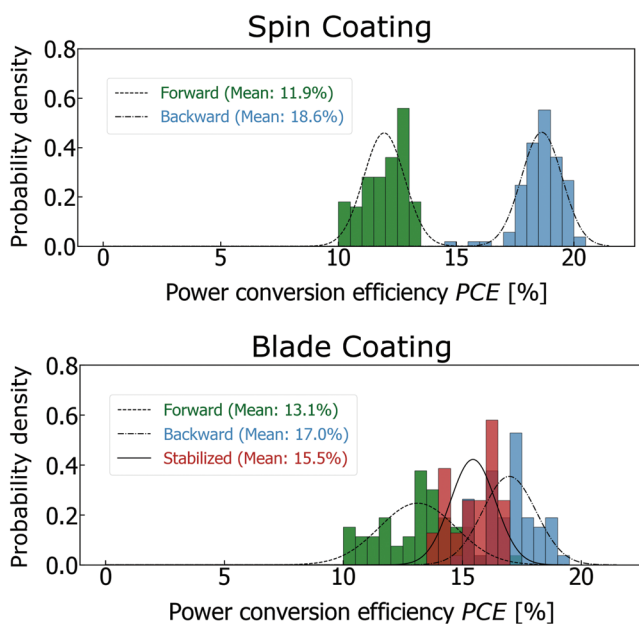


Figure 8. Probability density of the measured solar cell PCEs fitted with a normal distribution. The PCEs of the blade coated devices were gathered from all experiments with 2 m s^{-1} air velocity. While the PCE measured from backward J - V scans of the spin coated substrates are significantly higher than the blade coated ones, the hysteresis is smaller in the blade coated solar cells such that the means of the PCEs (spin 15.3% and blade 15.1%) are comparable. For the blade coated solar cells, the stabilized efficiencies over 300 s were additionally measured.

PbCl_2 99,999% trace metal basis and PbAc_2 Lead(II) acetate trihydrate 99,999% trace metal basis for the PbI_2 ; MAI precursor the same lead concentration was chosen and PbI_2 99,999% trace metal bases was also purchased from Sigma Aldrich) onto the substrate edge close to the blade, the cover was placed back onto the channel and the blade was dragged over the substrate with the velocity of 8.3 mm s^{-1} . The gap between the substrate and the blade was fixed at $100 \mu\text{m}$. After the blade coating, each photodiode signal reached the base-level, indicating the completion of the drying process, and the perovskite film turned brown. The dried perovskite layers were then annealed for 10 min at the temperature of $115 \text{ }^\circ\text{C}$. Afterward, the substrates were broken into eight $16 \times 16 \text{ mm}^2$ substrates and only the four middle ones were chosen for further processing. By this means, the impact of irregularities were avoided in the end and start regions of the blade coated perovskite layers. Then, Spiro-MeOTAD solution—comprised of 80 mg Spiro-MeOTAD (Luminescence Technology) dissolved in 1 mL chlorobenzene doped with $28.5 \mu\text{L mL}^{-1}$ of 4-*tert* butylpyridine and with $17.5 \mu\text{L}$ of lithium bis(trifluoromethanesulfonyl) imide from a stock solution of 520 mg mL^{-1} in acetonitrile—was spin coated with 4000 rpm for 30 s onto the perovskite-coated substrates. The Spiro-coated substrates were then exposed 12–15 h to air ($\approx 30\%$ humidity) for oxygen doping. Subsequently, 60 nm thick Au-electrodes were evaporated with a shadow mask in a Vactec Coat 320 thermal evaporator with a respective active area of 0.105 cm^2 and four individual solar cells per substrate. The spin coated solar cells were fabricated analogously with the same coating parameters, but they were cleaved into $16 \times 16 \text{ mm}^2$ before the coating of the ETL. The concentration of the perovskite precursor was in this case 1 mol mL^{-1} and the spin coating of the perovskite layer was performed with 3000 rpm for 30 s after dripping $40 \mu\text{L}$ solution onto each small substrate. The spin coated precursor layers were left for convective drying in the glove box for 7 min before the annealing step that had the same parameters as in the blade coated layers. SEM images of cross section of perovskite solar cells, with perovskite absorber layers

prepared for the parameters sets ($25 \text{ }^\circ\text{C}$, 0.02 m s^{-1} and $25 \text{ }^\circ\text{C}$, 0.2 m s^{-1}) are shown in Figure S20 (Supporting Information).

Morphology and Device Characterization: The perovskite layers as produced by the gas flow-assisted blade coating were examined by scanning electron and atomic force microscopy. Both techniques were used complementarily to determine the pinhole density (see Figure 5). The J - V characteristics of the devices were measured under a xenon-lamp-based solar simulator (Newport Oriol Sol3A) providing an airmass 1.5 global (AM1.5G) spectra at 100 mW cm^{-2} and calibrated by a silicon reference cell. The stable power output of the PSCs was determined by applying constant voltage at the maximum power point of the backward J - V scan under continuous AM1.5G illumination. A Peltier element was used to stabilize the temperature of the solar cells at $25 \text{ }^\circ\text{C}$ during all measurements, following the design of Schwenzer et al.^[79]

Supporting Information

Supporting Information is available from the Wiley Online Library or from the author.

Acknowledgements

The authors gratefully acknowledge financial support of the German Federal Ministry of Education and Research (PRINTPERO, funding code: 03SF0557A), the Initiating and Networking funding of the Helmholtz Association (HYIG of U.W.P. (funding code: VH-NG1148); Recruitment Initiative of B.S.R.; the Helmholtz Energy Materials Foundry (HEMF); PEROSEED (funding code: ZT-0024); and the Science and Technology of Nanostructures Research Program), and the KarlsruheSchool of Optics & Photonics (KSOP). The authors would like to thank the whole 'perovskite task force' at KIT, and in particular Tobias Abzieher for providing and organizing the main part of the lab infrastructure. Furthermore, the authors would like to express gratitude to the workshop staff of the Institute of Thermal Processing at KIT and for Schmidt-Hansberg et al. for building the foundation of the methods and setups presented herein. The authors are also grateful for Richard Thelen's support in AFM imaging and Anja Eberhardt for support with SEM Imaging. The authors would like to thank Margit Morvay for administration at the Institute of Thermal Processing.

Conflict of Interest

The authors declare no conflict of interest.

Keywords

blade coating, crystallization, drying control, in situ, perovskite solar cells

Received: May 14, 2019
Revised: August 2, 2019
Published online: August 27, 2019

- [1] G. Xing, N. Mathews, S. Sun, S. S. Lim, Y. M. Lam, M. Grätzel, S. Mhaisalkar, T. C. Sum, *Science* **2013**, 342, 344.
- [2] S. D. Stranks, G. E. Eperon, G. Grancini, C. Menelaou, M. J. P. Alcocer, T. Leijtens, L. M. Herz, A. Petrozza, H. J. Snaith, *Science* **2014**, 342, 341.
- [3] M. A. Green, A. Ho-Baillie, H. J. Snaith, *Nat. Photonics* **2014**, 8, 506.

- [4] M. Saliba, T. Matsui, J. Y. Seo, K. Domanski, J. P. Correa-Baena, M. K. Nazeeruddin, S. M. Zakeeruddin, W. Tress, A. Abate, A. Hagfeldt, M. Grätzel, *Energy Environ. Sci.* **2016**, *9*, 1989.
- [5] L. K. Ono, E. J. Juarez-Perez, Y. Qi, *ACS Appl. Mater. Interfaces* **2017**, *9*, 30197.
- [6] M. Saliba, T. Matsui, K. Domanski, J. Y. Seo, A. Ummadisingu, S. M. Zakeeruddin, J. P. Correa-Baena, W. R. Tress, A. Abate, A. Hagfeldt, M. Grätzel, *Science* **2016**, *354*, 206.
- [7] T. Duong, Y. L. Wu, H. Shen, J. Peng, X. Fu, D. Jacobs, E. C. Wang, T. C. Kho, K. C. Fong, M. Stocks, E. Franklin, A. Blakers, N. Zin, K. McIntosh, W. Li, Y. B. Cheng, T. P. White, K. Weber, K. Catchpole, *Adv. Energy Mater.* **2017**, *7*, 1.
- [8] Q. Jiang, Z. Chu, P. Wang, X. Yang, H. Liu, Y. Wang, Z. Yin, J. Wu, X. Zhang, J. You, *Adv. Mater.* **2017**, *29*, 1703852.
- [9] K. X. Steirer, P. Schulz, G. Teeter, V. Stevanovic, M. Yang, K. Zhu, J. J. Berry, *ACS Energy Lett.* **2016**, *1*, 360.
- [10] H. Zhu, K. Miyata, Y. Fu, J. Wang, P. P. Joshi, D. Niesner, K. W. Williams, S. Jin, X.-Y. Zhu, *Science* **2016**, *353*, 1409.
- [11] S. De Wolf, J. Holovsky, S. J. Moon, P. Löper, B. Niesen, M. Ledinsky, F. J. Haug, J. H. Yum, C. Ballif, *J. Phys. Chem. Lett.* **2014**, *5*, 1035.
- [12] A. Leguy, P. Azarhoosh, M. I. Alonso, M. Campoy-Quiles, O. J. Weber, J. Yao, D. Bryant, M. T. Weller, J. Nelson, A. Walsh, M. van Schilfgaarde, P. R. F. Barnes, *Nanoscale* **2016**, *8*, 6317.
- [13] H. Zhu, Y. Fu, F. Meng, X. Wu, Z. Gong, Q. Ding, M. V. Gustafsson, M. T. Trinh, S. Jin, X.-Y. Zhu, *Nat. Mater.* **2015**, *14*, 636.
- [14] H. Wei, Y. Fang, P. Mulligan, W. Chuirazzi, H.-H. Fang, C. Wang, B. R. Ecker, Y. Gao, M. A. Loi, L. Cao, J. Huang, *Nat. Photonics* **2016**, *10*, 333.
- [15] P. Brenner, T. Glöckler, D. Rueda-Delgado, T. Abzieher, M. Jakoby, B. S. Richards, U. W. Paetzold, I. A. Howard, U. Lemmer, *Opt. Mater. Express* **2017**, *7*, 4082.
- [16] J. W. Lee, Y. J. Choi, J. M. Yang, S. Ham, S. K. Jeon, J. Y. Lee, Y. H. Song, E. K. Ji, D. H. Yoon, S. Seo, H. Shin, G. S. Han, H. S. Jung, D. Kim, N. G. Park, *ACS Nano* **2017**, *11*, 3311.
- [17] C. Prall, C. Kaspari, F. Brunner, K. Haberland, M. Weyers, D. Rueter, *J. Cryst. Growth* **2015**, *415*, 1.
- [18] J.-P. Correa-Baena, A. Abate, M. Saliba, W. Tress, T. Jesper Jacobsson, M. Grätzel, A. Hagfeldt, *Energy Environ. Sci.* **2017**, *10*, 710.
- [19] A. Kojima, K. Teshima, Y. Shirai, T. Miyasaka, *J. Am. Chem. Soc.* **2009**, *131*, 6050.
- [20] NREL, "NREL Efficiency chart," <https://www.nrel.gov/pv/cell-efficiency.html> (accessed: August 2019).
- [21] J. Seo, J. H. Noh, S. Il Seok, *Acc. Chem. Res.* **2016**, *49*, 562.
- [22] S. Yang, W. Fu, Z. Zhang, H. Chen, C. Z. Li, *J. Mater. Chem. A* **2017**, *5*, 11462.
- [23] W. Tress, *Adv. Energy Mater.* **2017**, *7*, 1602358.
- [24] H. Chen, X. Ding, X. Pan, T. Hayat, A. Alsaedi, Y. Ding, S. Dai, *J. Power Sources* **2018**, *402*, 82.
- [25] I. A. Howard, T. Abzieher, I. M. Hossain, H. Eggers, F. Schackmar, S. Ternes, B. S. Richards, U. Lemmer, U. W. Paetzold, *Adv. Mater.* **2019**, *31*, 1806702.
- [26] S. Razza, S. Castro-Hermosa, A. Di Carlo, T. M. Brown, *APL Mater.* **2016**, *4*, 091508.
- [27] T. M. Schmidt, T. T. Larsen-Olsen, J. E. Carlé, D. Angmo, F. C. Krebs, *Adv. Energy Mater.* **2015**, *5*, 1.
- [28] Y. Galagan, F. Di Giacomo, H. Gortler, G. Kirchner, I. de Vries, R. Andriessen, P. Groen, *Adv. Energy Mater.* **2018**, *8*, 1801935.
- [29] J. B. Whitaker, D. H. Kim, B. W. Larson, F. Zhang, J. J. Berry, M. F. A. M. van Hest, K. Zhu, *Sustainable Energy Fuels* **2018**, *2*, 2442.
- [30] G. Cotella, J. Baker, D. Worsley, F. De Rossi, C. Pleydell-Pearce, M. Carnie, T. Watson, *Sol. Energy Mater. Sol. Cells* **2017**, *159*, 362.
- [31] J. Huang, *Mater. Horiz.* **2015**, *2*, 578.
- [32] Y. Deng, E. Peng, Y. Shao, Z. Xiao, Q. Dong, J. Huang, *Energy Environ. Sci.* **2015**, *8*, 1544.
- [33] S. T. Williams, A. Rajagopal, C. C. Chueh, A. K. Y. Jen, *J. Phys. Chem. Lett.* **2016**, *7*, 811.
- [34] F. Di Giacomo, A. Fakharuddin, R. Jose, T. M. Brown, *Energy Environ. Sci.* **2016**, *9*, 3007.
- [35] L. L. Gao, C. X. Li, C. J. Li, G. J. Yang, *J. Mater. Chem. A* **2017**, *5*, 1548.
- [36] L. L. Gao, K. Zhang, N. Chen, G. J. Yang, *J. Mater. Chem. A* **2017**, *5*, 18120.
- [37] M. Kohlstädt, M. A. Yakoob, U. Würfel, *Phys. Status Solidi A* **2018**, *215*, 1.
- [38] Q. Hu, L. Zhao, J. Wu, K. Gao, D. Luo, Y. Jiang, Z. Zhang, C. Zhu, E. Schaible, A. Hexemer, C. Wang, Y. Liu, W. Zhang, M. Grätzel, F. Liu, T. P. Russell, R. Zhu, Q. Gong, *Nat. Commun.* **2017**, *8*, 15688.
- [39] D. Lee, Y.-S. Jung, Y.-J. Heo, S. Lee, K. Hwang, Y.-J. Jeon, J.-E. Kim, J. Park, G. Y. Jung, D.-Y. Kim, *ACS Appl. Mater. Interfaces* **2018**, *10*, 16133.
- [40] J. Ding, Q. Han, Q. Q. Ge, D. J. Xue, J. Y. Ma, B. Y. Zhao, Y. X. Chen, J. Liu, D. B. Mitzi, J. S. Hu, *Joule* **2019**, *3*, 402.
- [41] H. Hu, Z. Ren, P. W. K. Fong, M. Qin, D. Liu, D. Lei, X. Lu, G. Li, *Adv. Funct. Mater.* **2019**, *29*, 1900092.
- [42] Y. Zhong, R. Munir, J. Li, M. Tang, M. R. Niazi, D. Smilgies, K. Zhao, A. Amassian, *ACS Energy Lett.* **2018**, *3*, 1078.
- [43] Q. Wang, M. Eslamian, T. Zhao, A. K.-Y. Jen, *IEEE J. Photovoltaics* **2018**, *8*, 1662.
- [44] Y. Deng, Q. Dong, C. Bi, Y. Yuan, J. Huang, *Adv. Energy Mater.* **2016**, *6*, 1600372.
- [45] S. Tang, Y. Deng, X. Zheng, Y. Bai, Y. Fang, Q. Dong, H. Wei, J. Huang, *Adv. Energy Mater.* **2017**, *7*, 1700302.
- [46] J. Li, R. Munir, Y. Fan, T. Niu, Y. Liu, Y. Zhong, Z. Yang, Y. Tian, B. Liu, J. Sun, D. M. Smilgies, S. Thoroddsen, A. Amassian, K. Zhao, S. (Frank) Liu, *Joule* **2018**, *2*, 1313.
- [47] W. Kong, G. Wang, J. Zheng, H. Hu, H. Chen, Y. Li, M. Hu, X. Zhou, C. Liu, B. N. Chandrashekar, A. Amini, J. Wang, B. Xu, C. Cheng, *Sol. RRL* **2018**, *2*, 1700214.
- [48] F. Mathies, H. Eggers, B. S. Richards, G. Hernandez-Sosa, U. Lemmer, U. W. Paetzold, *ACS Appl. Energy Mater.* **2018**, *1*, 1834.
- [49] F. X. Xie, D. Zhang, H. Su, X. Ren, K. S. Wong, M. Grätzel, W. C. Choy, *ACS Nano* **2015**, *9*, 639.
- [50] X. Li, D. Bi, C. Yi, J.-D. Decoppet, J. Luo, S. M. Zakeeruddin, A. Hagfeldt, M. Grätzel, *Science* **2016**, *353*, 58.
- [51] M. Yang, Z. Li, M. O. Reese, O. G. Reid, D. H. Kim, S. Siol, T. R. Klein, Y. Yan, J. J. Berry, M. F. A. M. van Hest, K. Zhu, *Nat. Energy* **2017**, *2*, 17038.
- [52] J. J. van Franeker, K. H. Hendriks, B. J. Bruijnsaers, M. W. G. M. Verhoeven, M. M. Wienk, R. A. J. Janssen, *Adv. Energy Mater.* **2017**, *7*, 1601822.
- [53] L. Wagner, L. E. Mundt, G. Mathiazhagan, M. Mundus, M. C. Schubert, S. Mastroianni, U. Würfel, A. Hinsch, S. W. Glunz, *Sci. Rep.* **2017**, *7*, 14899.
- [54] D. P. Nenon, J. A. Christians, L. M. Wheeler, J. L. Blackburn, E. M. Sanehira, B. Dou, M. L. Olsen, K. Zhu, J. J. Berry, J. M. Luther, *Energy Environ. Sci.* **2016**, *9*, 2072.
- [55] J. S. Manser, M. I. Saidaminov, J. A. Christians, O. M. Bakr, P. V. Kamat, *Acc. Chem. Res.* **2016**, *49*, 330.
- [56] R. Munir, A. D. Sheikh, M. Abdelsamie, H. Hu, L. Yu, K. Zhao, T. Kim, O. El Tall, R. Li, D. M. Smilgies, A. Amassian, *Adv. Mater.* **2017**, *29*, 1604113.
- [57] D. T. Moore, H. Sai, K. W. Tan, D. M. Smilgies, W. Zhang, H. J. Snaith, U. Wiesner, L. A. Estroff, *J. Am. Chem. Soc.* **2015**, *137*, 2350.
- [58] V. L. Pool, B. Dou, D. G. Van Campen, T. R. Klein-Stockert, F. S. Barnes, S. E. Shaheen, M. I. Ahmad, M. F. A. M. van Hest, M. F. Toney, *Nat. Commun.* **2017**, *8*, 14075.
- [59] L. H. Rossander, T. T. Larsen-Olsen, H. F. Dam, T. M. Schmidt, M. Corazza, K. Norrman, I. Rajkovic, J. W. Andreasen, F. C. Krebs, *CrytEngComm* **2016**, *18*, 5083.

- [60] M. He, B. Li, X. Cui, B. Jiang, Y. He, Y. Chen, D. O'Neil, P. Szymanski, M. A. El-Sayed, J. Huang, Z. Lin, *Nat. Commun.* **2017**, *8*, 16045.
- [61] S. Tang, Y. Deng, X. Zheng, Y. Bai, Y. Fang, Q. Dong, H. Wei, J. Huang, *Adv. Energy Mater.* **2017**, *7*, 1700302.
- [62] M. Kohlstädt, M. A. Yakoob, U. Würfel, *Phys. Status Solidi A* **2018**, *215*, 1800419.
- [63] Y. Deng, X. Zheng, Y. Bai, Q. Wang, J. Zhao, J. Huang, *Nat. Energy* **2018**, *3*, 560.
- [64] L. L. Gao, K. J. Zhang, N. Chen, G. J. Yang, *J. Mater. Chem. A* **2017**, *5*, 18120.
- [65] M. Remeika, S. R. Raga, S. Zhang, Y. Qi, *J. Mater. Chem. A* **2017**, *5*, 5709.
- [66] B. Schmidt-Hansberg, H. Do, A. Colsmann, U. Lemmer, W. Schabel, *Eur. Phys. J.: Spec. Top.* **2009**, *166*, 49.
- [67] B. Schmidt-Hansberg, M. F. G. Klein, K. Peters, F. Buss, J. Pfeifer, S. Walheim, A. Colsmann, U. Lemmer, P. Scharfer, W. Schabel, *J. Appl. Phys.* **2009**, *106*, 124501.
- [68] B. Schmidt-Hansberg, M. Baunach, J. Krenn, S. Walheim, U. Lemmer, P. Scharfer, W. Schabel, *Chem. Eng. Process.* **2011**, *50*, 509.
- [69] B. Schmidt-Hansberg, M. Sanyal, M. F. G. Klein, M. Pfaff, N. Schnabel, S. Jaiser, A. Vorobiev, E. Müller, A. Colsmann, P. Scharfer, D. Gerthsen, U. Lemmer, E. Barrena, W. Schabel, *ACS Nano* **2011**, *5*, 8579.
- [70] K. L. Saenger, H. Tong, *J. Appl. Polym. Sci.* **1987**, *33*, 1777.
- [71] Y. Heights, *Polym. Eng. Sci.* **1991**, *37*, 432.
- [72] J. Bergqvist, S. A. Mauger, K. Tvingstedt, H. Arwin, O. Ingan, *Sol. Energy Mater. Sol. Cells* **2013**, *114*, 89.
- [73] J. J. van Franeker, D. Hermida-Merino, C. Gommès, K. Arapov, J. J. Michels, R. A. J. Janssen, G. Portale, *Adv. Funct. Mater.* **2017**, *27*, 1702516.
- [74] W. Qiu, T. Merckx, M. Jaysankar, C. Masse De La Huerta, L. Rakocevic, W. Zhang, U. W. Paetzold, R. Gehlhaar, L. Froyen, J. Poortmans, D. Cheyens, H. J. Snaith, P. Heremans, *Energy Environ. Sci.* **2016**, *9*, 484.
- [75] T. L. Bergman, A. S. Lavine, F. P. Incropera, D. P. Dewitt, *Fundamentals of Heat and Mass Transfer*, Wiley, New York **2011**.
- [76] VDI e. V., *VDI-Wärmeatlas*, Springer Vieweg, Berlin **2013**.
- [77] P. S. Whitfield, N. Herron, W. E. Guise, K. Page, Y. Q. Cheng, I. Milas, M. K. Crawford, *Sci. Rep.* **2016**, *6*, 35685.
- [78] J. Kong, Z. Bo, H. Yang, J. Yang, X. Shuai, J. Yan, K. Cen, *Phys. Chem. Chem. Phys.* **2017**, *19*, 7678.
- [79] J. A. Schwenzer, L. Rakocevic, R. Gehlhaar, T. Abzieher, S. Gharibzadeh, S. Moghadamzadeh, A. Quintilla, B. S. Richards, U. Lemmer, U. W. Paetzold, *ACS Appl. Mater. Interfaces* **2018**, *10*, 16390.